Results in Optics 12 (2023) 100480

Contents lists available at ScienceDirect

Results in Optics

journal homepage: www.sciencedirect.com/journal/results-in-optics

Higher order correction and spectral deconvolution of wavelength-resolved neutron transmission imaging at the CONRAD-2 instrument

Ala'a Al-Falahat[a,*], Nikolay Kardjilov[b], Talib K. Murtadha[a], Robin Woracek[c], Saad Alrwashdeh[a], Ingo Manke[b]

[a] Department of Mechanical Engineering, Mutah University, Mutah, Al-Karak 61710 P.O. Box 7, Jordan
[b] Helmholtz-Zentrum Berlin, Hahn-Meitner-Platz 1, Berlin 14109, Germany
[c] European Spallation Source ERIC, PO Box 176, Lund 22100, Sweden

ARTICLE INFO

Keywords:
Fourier self-deconvolution
Wavelength resolution
Higher order scattering
Transmission spectroscopy
Crystallographic phases
Bragg edge

ABSTRACT

This paper uses a Fourier self-deconvolution method for improving the wavelength resolution in transmission experiments at continuous neutron sources utilizing a double-crystal monochromator device to probe as well as correct the generation of higher-order neutron scattering in a monochromatic neutron beam. The cold neutron radiography CONRAD-2 equipment has been utilized to resolve the steel transmission spectra of changing BCC phase and FCC phase fractions. Therefore, both low and high-spectral resolution instruments with equivalent wavelength resolution have been proposed. The primary benefit of Fourier self-deconvolution is its ability to precisely narrow individual bands without modifying their relative position or the total band area. Thus, the resolution of the transmission spectrum has been improved by a factor of 3.16, and the info that the sample material comprises two crystallographic phases has been determined by the wavelength resolution improvement employing the deconvolution approach. Additionally, the slight variation in Bragg edge position for different phase fractions and the locations of the double phase Bragg edges have also been obtained using the ray-tracing simulation tool McStas. The high resolution neutron wavelength selection experiment with the ESS test_beamline (V20) instrument employing the neutron time-of-flight detection demonstrates the precision of the resolving steel Bragg edge.

1. Introduction

Neutrons are a very adaptable tool for studying the underlying structure of materials. There are many applications for neutron sources, including but not limited to physics, engineering, medicine, nuclear weapons, petroleum exploration, biology, chemistry, and nuclear power.

Since the neutron has no electrical charge, it can pass through matter freely and provide a reliable evidence of its bulk properties. Even with X-ray, which is generally regarded as a bulk method, the wavelength supplied by a laboratory X-ray tube limits the penetration to a few hundred nanometers at most.

Neutron scattering is a valuable tool in science and technology that reveals insights into the most basic characteristics of condensed matter (Alrwashdeh et al., 2022; Alrwashdeh et al., 2016). The available neutron flux is the determining factor in the quality and accuracy of neutron scattering experiments. This is done at spallation neutron sources and research reactors that produce a strong enough neutron radiation for this purpose.

The high spectral resolution is useful for making fine-grained comparisons over large wavelength intervals. Ultimately, the spectral resolution can give images with their real colors, while the spatial resolution allows the scientists to analyze the images in high visual detail. In the product quality assurance operations, medical sample testing and forensic sample testing, both spatial and spectral resolutions are necessary for a comprehensive analysis of test samples.

The maximum spectral resolution is practically limited by the instrumental resolution, where the resolution of the neutron spectrum is defined in this study as the ratio of the experimentally-measured Bragg edge wavelength to the full width half maximum FWHM of the profile ($\Delta\lambda/\lambda$) (Al-Falahat et al., 2019). Some instruments utilize a lower spectrum resolution (broader spectral transmission profile) to shorten the experimental time. However, the need for a spectrum without artificial peaks is desired for extracting maximum info from the

* Corresponding author.
E-mail address: alaa.falahat@mutah.edu.jo (A. Al-Falahat).

https://doi.org/10.1016/j.rio.2023.100480
Received 8 January 2023; Received in revised form 1 May 2023; Accepted 29 June 2023
Available online 5 July 2023
2666-9501/© 2023 Published by Elsevier B.V. This is an open access article under the CC BY-NC-ND license (http://creativecommons.org/licenses/by-nc-nd/4.0/).

investigational data. It is essential to identify the error sources not only in the investigational spectrum collection but also in the post processing performance (Ala'a, 2019; Al-Falahat et al., 2019) using a methodology of growing popularity that employs the Fourier deconvolution (Mantsch et al., 1988; Kauppinen et al., 1981; Rahmelow and Huebner, 1996) to enhance the spatial resolution.

The Fourier self-deconvolution technique employs the Fourier transform to improve the spectral resolution of the instrument contaminated by γ photons, and the fast neutrons provide good conditions for the spectral readings.

Experiments with neutron wavelength selective transmission spectra are undertaken to analyze the samples with a thicknesses of several cm to learn more about the potential benefit of the deconvolution process. According to Bragg's law, which is based on the neutron transmission profile, the so-called Bragg edges appear in polycrystalline samples at wavelength locations lambda (λ), equal two times the lattice plane distances (d_{hkl}). Thus, the neutron Bragg edge imaging is performed by taking radiography pictures prior and beyond a Bragg edge to achieve a contrast relating to the crystallographic features. This research also aims to provide the basis for the use of mathematical algorithms that permit the separation of Bragg edges that would otherwise overlap.

Numerous studies have manifested that the quantitative determinations of crystallographic phase fractions are possible in the transmission measurements, making the neutron transmission a more appealing method for retrieving the crystallographic phases. Early experimental results for the reversed-phase transformation in the austenitic stainless steel were compared using neutron diffraction and transmission in (Al-Falahat et al., 2019; Al-Falahat et al., 2022; Tran et al., 2022; Tran et al., 2023).

Each phase of a polycrystalline material has its own unique set of Bragg edges, which can occur at a wide range of wavelengths and imply considerably different attenuation coefficients. In theory, it is possible to distinguish between and quantify two or more phases using only monochromatic data. In practice, however, it is often necessary to record a Bragg edge spectrum covering a wider wavelengths range for one or more Bragg edges of every phase. And, this gives a vision when, for example, the sample depicts or forms an important texture or a porosity change during a phase transition, which could further complicate a phase determination.

A cold neutron radiography instrument (CONRAD-2) at the BER II research reactor of Helmholtz-Zentrum Berlin (HZB) in Germany was used for this manuscript's experiments. CONRAD-2 provides a relatively low wavelength resolution of roughly 1.36% for a crystal mosaicity of 0.8°, and more quantitative details about the neutron wavelength resolution are described in (Al-Falahat et al., 2019), on the other hand, the results with the Time of Flight (TOF) method at the ESS Test Beamline (TBL) instrument, which offers a considerably superior wavelength resolution (below 1%), are also presented.

This paper is organized into several parts, starting with an introduction followed by the deconvolution theory of the neutron spectrum, and then the experimental part is presented by CONRAD-2 instrument at a respective low resolution by using steel samples at varying amounts of microstructure, including martensite (BCC) and austenite (FCC) crystallography. Therefore, the neutron transmission profile of the steel sample is recorded, and after that, the correction of the transmission spectrum of the CONRAD-2 instrument is performed to get rid of the double crystal monochromator contamination of the intensity of 1st-order wavelength by higher orders. In the next part, the neutron wavelength resolution which is recorded by the CONRAD-2 instrument is enhanced by using the deconvolution method.

In addition, the corrected and enhanced transmission spectrum is compared with the transmission spectrum that is recorded by using an ESS instrument at a high wavelength resolution. Also, the ray-tracing modeling tool McStas is built up to simulate the neutron transmission at particular instruments providing clarity to the steel transmission spectra of both BCC and FCC phases. Finally, the section of conclusion is presented.

2. Deconvolution theory

The spectrum of recorded neutron intensity $I(\lambda)$ can be modeled as a broadening function $I_o(\lambda)$ convolution with a higher-resolution spectrum $I^{'}(\lambda)$, where

$$I(\lambda) = I_o(\lambda) \times I^{'}(\lambda), \tag{1}$$

By using this deconvolution method, one can extract the function $I^{'}(\lambda)$ from Eq. (1). The deconvoluted spectrum $I^{'}(\lambda)$ can be stated using the frequency convolution theorem (Mantsch et al., 1988; Kauppinen et al., 1981; Griffiths and Pariente, 1986) as:

$$I^{'}(\lambda) = F^{-1}\left\{\frac{D(x)I(x)}{I_o(x)}\right\}, \tag{2}$$

Where:

F^{-1} : The inverse Fourier transform.

$D(x)$: The well-known apodization function, which is utilized for minimizing the side-lobes amplitude in the deconvoluted spectrum; that means producing the ultimate enhancement in the spectrum via smoothing the data which $D(x) \neq 0$. Hence, the function becomes unity if $\times = 0$ and drops to (0) if $\times$ is equal to (1) (Kauppinen et al., 1981; Kauppinen et al., 1981).

$I_o(x)$: The Fourier transform (FT) of the broadening function $I_o(\lambda)$, where $I(x)$ defines the bands' intrinsic line shape. Also, there're different methods to the interferogram $I_o(x)$ employed as a deconvolution function in this study, and the Lorentzian line form function is applied.

$$I_o(\lambda) = \frac{1}{\pi}\frac{\gamma^{'}}{(\gamma^{'2} + \lambda^2)} \tag{3}$$

Where, $\gamma^{'}$ is the HWHM of the fresh spectrum band. When one considers the HWHM band origin to be γ_i, then the HWHM will be minimized to $(\gamma_i - \gamma^{'})$. It's also observed that every band area is unaffected, and every band $(A_i^0)^{'}$ peak is thus augmented to a value given via:

$$(A_i^0)^{'} = A_i^0 \frac{\gamma_i}{(\gamma_i - \gamma^{'})} \tag{4}$$

The HWHM ratio prior and beyond the deconvolution, $\gamma_i/(\gamma_i - \gamma^{'})$, is named the resolution improvement factor (k) (Kauppinen et al., 1981).

For the data analysis introduced in this work, the OriginLab software (OriginLab) performs Fourier deconvolutions on the data. And, the utilized deconvolution routine is depended upon the theory characterized upstairs and it can be conducted via changing (2) factors: "$\gamma^{'}$" as well as "smoothing factor X".Where, $\gamma^{'}$ is the quantity via which the FWHM is minimized, and the smoothing factor (X) is utilized for smoothing the deconvoluted spectrum which has to be between zero and one. Also, the bigger the $\gamma^{'}$, the better the band narrowing is, and the bigger the smoothing factor (X), the smoother the deconvoluted spectrum is. The two factors have to be varied at the same time for optimizing the resolution improvement process and for minimizing the deconvolution artifacts as well as distortions (Griffiths and Pariente, 1986).

3. Experiment with the cold neutron radiography apparatus (CONRAD-2) at a low wavelength resolution

An experiment was carried out using a double crystal monochromator (Kardjilov et al., 2016; Kardjilov et al., 2016). A steel sample was positioned a few cm ahead of a ^{6}LiF/Zns scintillator screen of a (10 μm) thickness detector.

The purpose of the detector is to convert the conveyed neutrons into noticeable light, and an optical charge coupled device (CCD) camera with an objective lens (Kardjilov et al., 2011; Tötzke et al., 2011). And,

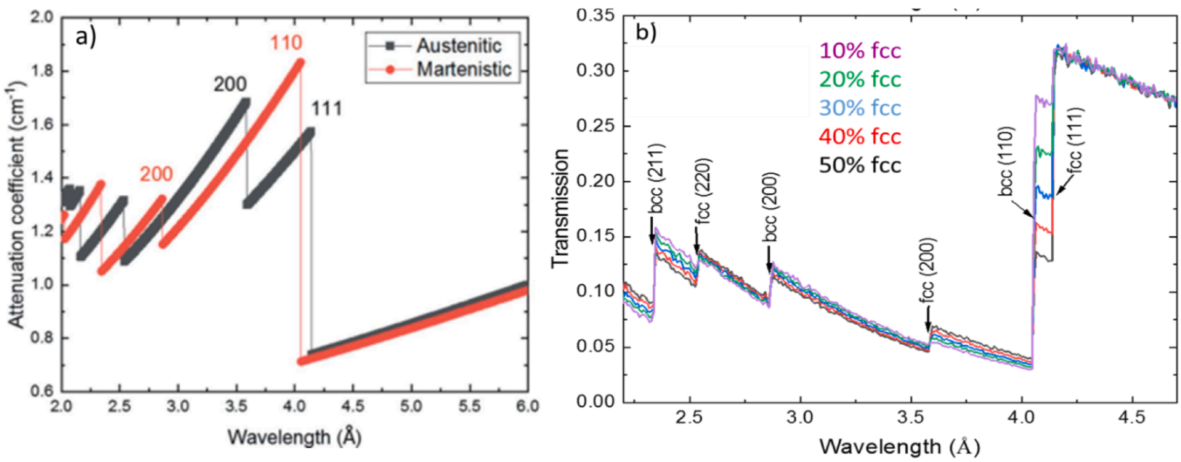

Fig. 1. (a) Comparing the attenuation coefficient of the martensitic structure (BCC) and the austenitic structure (FCC) as calculated using the nxsPlotter software (Al-Falahat et al., 2022). (b) Simulation Bragg edge spectra for a (10 mm) thick steel sample with the phases of BCC and FCC at a varying percentage of steel phases.

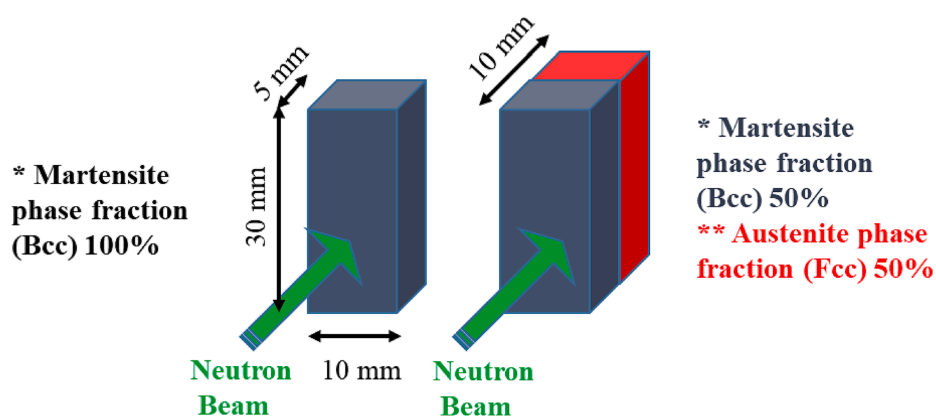

Fig. 2. Schematic of a sample composed of martensite and austenite phases and their orientation in the neutron beam.

the presented data has an effective pixel dimension of (55 μm), with a Field of View (FOV) of (11.1 × 11.1 cm^2). More technical details can be found elsewhere (Kardjilov et al., 2016).

The crystallographic body-centered cubic structure of α-ferrite and α'-martensite in the material under study is identical. Therefore, the Bragg-edge diagram cannot differentiate between α'-martensite and α-ferrite, therefore α-ferrite is utilized to compute the α'-martensite's theoretical attenuation values (Woracek et al., 2018).

For clarifying the steel transmission spectra of the BCC and FCC phases, the simulations of Bragg edges for a steel sample with a (20 mm) thickness was carried out via employing a McStas software (Nielsen and Lefmann, 2000), as revealed in Fig. 1a. Additionally, the dual phase Bragg edges locations for various phase fractions were obviously specified, and the small shift in the Bragg edge location was at about (4.2 Å). The spectra with Bragg edge positions from the austenite phase using varying fractions of FCC (10%, 20%, 30%, 40%, and 50%) are displayed in the Fig. 1b. Also, the dual phase Bragg edges locations for various fractions were specified, as the small shift in the Bragg edge location was at about (4.1 Å). The researchers' attention was drawn to the highest Bragg edges at around (4.1 Å), where the location of the shoulder-like Bragg edge transmission spectrum can be altered via changing the ratio of BCC to FCC phases. As a result, there is a greater change in the Bragg edge's position when the fraction of the FCC crystal structure is reduced.

For two-phased steel mixes, the present work's simulations demonstrated the influence of the BCC phase close to the FCC phase at (4.1 Å), which explains the corresponding experimental Bragg edge shape and

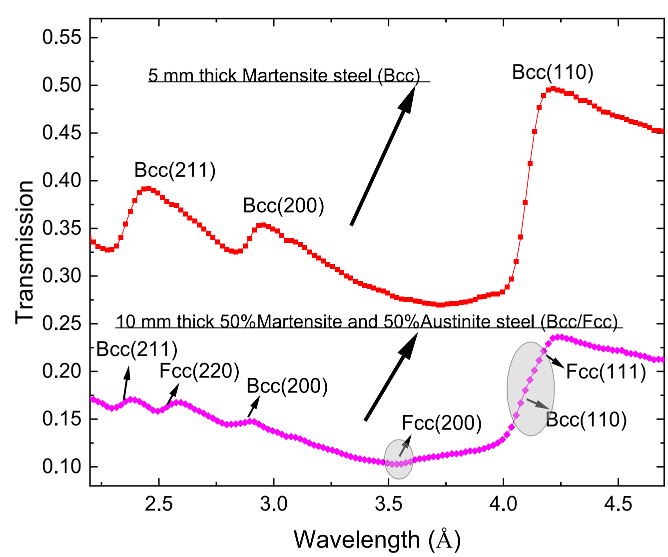

Fig. 3. Neutron transmission spectrum of the BCC and FCC steel crystallographic phases. Samples are 5 and 10 mm thick, respectively. Data were measured at CONRAD-2, at 10 mm thick showing the change in Bragg edge shape and height due to the presence of two phases at 4.1 Å.

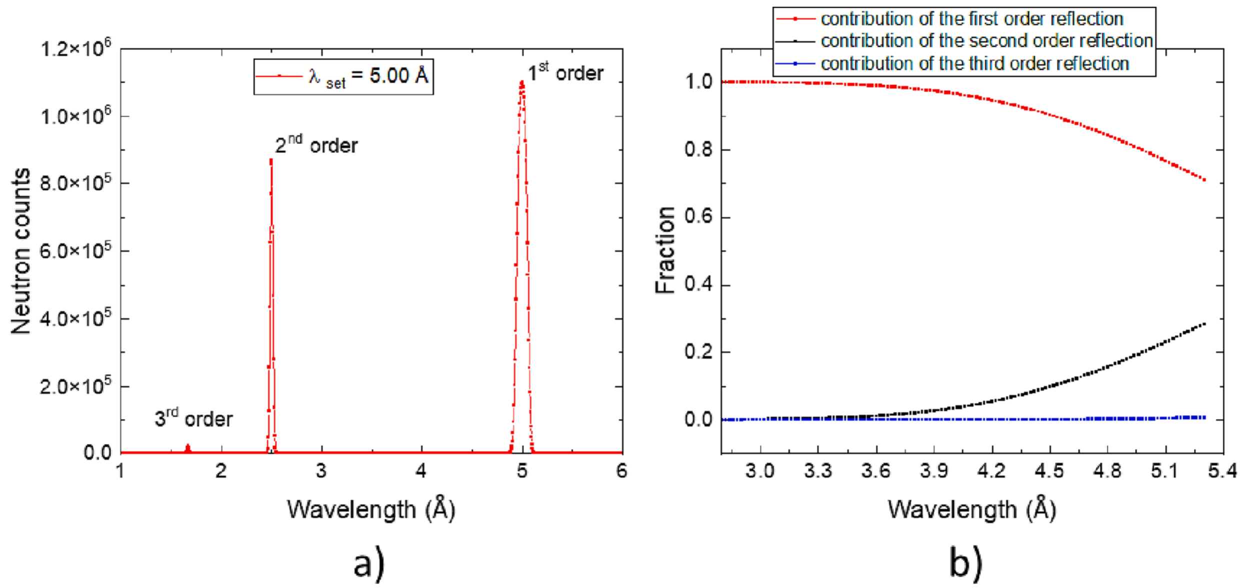

Fig. 4. (a) The recorded 1st and higher order reflections for the CONRAD-2 spectrum when using the dual crystal monochromator at (5 Å). (b) The comparative contribution of the higher order components to the entire no. of neutrons modeled employing McStas software.

position with a sample of the same phase ratio.

However, the material that is utilized is steel which includes varying amounts of microstructure, including martensite (BCC) and austenite (FCC) crystallography, as seen in Fig. 2. The sample dimensions are 10 mm in length, 30 mm in height, and 5 mm in thickness. Martensite and austenite plates were manufactured and stacked to set different martensite/austenite phase fractions in the neutron transmission path.

The transmission of neutron throughout the sample was measured at every step of wavelength scan from (2.0 Å) to (4.8 Å) using (20 sec) exposure duration at CONRAD-2. The transmission was determined after the open beam and dark field images of the sample were used to normalize the raw radiographs and therefore remove the beam spatial inhomogeneity. Images were analyzed with the help of the program ImageJ (Abràmoff et al., 2004). For maximizing the intensity of signal (for quicker measurements) as well as decreasing the noise, a region of interest (ROI) with overall dimensions of (91 mm × 33 mm) was chosen for the reported results.

Fig. 3 displays a plot of the wavelength-dependent neutron transmission throughout the sample and it also reveals the Bragg edge spectrum gaining at CONRAD-2, with a (5 mm) thickness almost pure

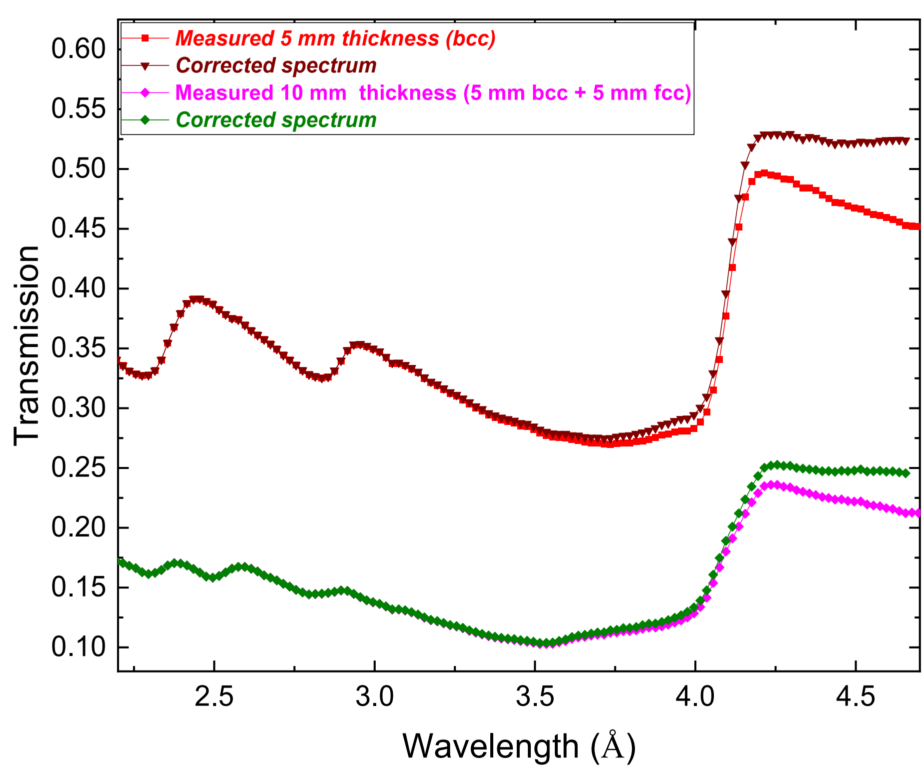

Fig. 5. Measured and corrected neutron wavelength transmission profiles at CONRAD-2 for a (5 mm) thick pure martensite (BCC phase) and two combined (5 mm) thick samples with a BCC and FCC steel structure, respectively.

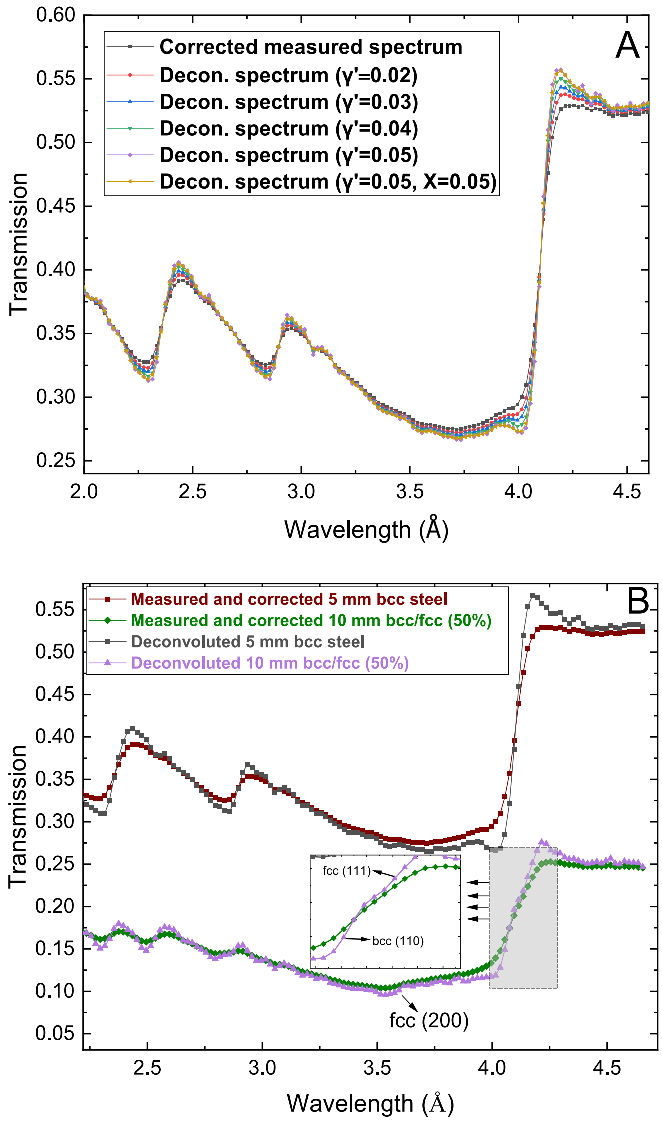

Fig. 6. (A) A series of progressively deconvoluted spectra of corrected sample Bragg edges measured at CONRAD-2 using increasing γ' (0.02, 0.03, 0.04, and 0.05) as well as the factor of smoothing (X = 0.02). (B) The measured deconvolution spectra of the steel samples at CONRAD-2.

BCC martensite crystallography Bargg's edges (red curve), a (10 mm) thickness staked as 50% of BCC martensite phase as well as 50% of FCC austenite phase (purple curve), and combined austenite and martensite phases, exhibiting the FCC (111), FCC (200), FCC (220) Bragg edges, BCC (110), BCC (200), and BCC (211) Bragg edges. As a result, a similar experimental strategy can be used to map the various phase fractions (Woracek et al., 2018).

The neutron transmission spectrum is broadening as a result of instrument resolution, which impacts the wavelength resolution of the spectrum, as evinced by the analysis of the cut-off Bragg edge at around (4.1 Å), which should undergo a minor shift through the height of its Bragg edge due to a change in the crystalline phase fraction, from 50% austenite BCC phase to 50% martensite FCC phase, as elucidated in Fig. 3.

4. Correction of neutron transmission spectrum

According to Bragg's law ($2d_{hkl}sin\theta = n\lambda$), a crystal monochromator that is tuned to reflect a specific wavelength lambda (λ) in the orientation angle $2\theta_n$ from a set of crystal lattice planes d_{hkl} will also reflect neutrons with wavelengths λ/2, λ/3….and λ/n, resulting in 2nd, 3rd,… and n[th] order contamination in the monochromatized beam.

So, McStas software (Willendrup and Lefmann, 2020) was used to model the monochromatic neutron beam from the Highly Oriented Pyrolytic Graphite (HOPG) crystal (mosaic spread = 0.8) as well as its reflections higher order for the neutron wavelength range available at CONRAD-2.

Fig. 4a displays the neutron counts at (5 Å) for a monochromatic beam recording the first, second, and third orders of reflections. There is a degree of contamination of the intensity of 1st-order wavelength by the higher orders (2nd and 3rd-order of reflections).

Fig. 4b portrays the comparative contributions of the 1st and higher orders of reflections over a wavelength range of (2.8–5.3 Å). The fraction of the second order reflection that impacts the first order reflection begins at (3.3 Å) and continues to increase at longer wavelengths. For instance, at (5.3 Å), over (28%) of the total contribution comes from the second order of reflection. The intense neutron transmission from the higher-order contaminations is therefore negligible at shorter wavelengths up to about (3.3 Å) but becomes significant at longer wavelengths. Specifically, the intensity contribution from the second order of reflection (λ/2) should be corrected by removing the higher order beam components, resulting in a corrected transmission spectrum, as shown in Fig. 5.

5. Enhancement of the measured wavelength resolution

The unconvoluted CONRAD-2 spectrum resolves the broad Bragg edges location, where the distinct features' influence of both BCC and FCC phases cannot be specified at (4.1 Å), as illustrated in Fig. 6. So, utilizing the deconvolution process characterized overhead, the wavelength resolution of the spectra taken at the CONRAD-2 device can be improved.

A series of deconvoluted Bragg-edge spectra is shown in Fig. 6a, where the resolution is highly enhanced via employing the resolution improvement method in comparison with the initial spectrum. Because there's usually a noise existing in the investigational spectrum, the characteristic side lobes appearance is noted at about (4 Å) for $\gamma' = 0.06$. For the side lobes commonly, one uses the term over-deconvolution since the deconvoluted values are not real because they do not exist in the spectrum for $\gamma'(0.02 \text{ and } 0.04)$. Thus, the side lobes appearance relies upon the deconvolution strength as it raises by the γ' value increase. Moreover, a small possible value of the filter has to be utilized for obtaining a comparable degree of the deconvoluted spectrum smoothing in comparison with the initial spectrum.

Selection of the optimum factors of deconvolution is significant for such kind of spectral analysis. And, in the method of present work, the deconvolution degree was obtained via the two factors values: $\gamma' = 0.065$, and a smaller filter value has to be utilized for obtaining a comparable smoothing degree in comparison with the initial spectrum. Here, X equal to (0.02) is chosen, as seen in Fig. 6b. Also, the resolution improvement factor (K) is 3.16, that means the deconvolution method raises the CONRAD-2 device's wavelength resolution via a (3.16) factor. As well, the Bragg edge FWHM was obtained via the nonlinear least-squares fitting. Additionally, the transmission spectrum derivative was taken, and a Gaussian fit was implemented.

From a theoretical view point, it would be optimum to choose a γ' value that's as big as possible, matching to the spectrum resolution. Nonetheless, in the practice, the uppermost attainable resolution improvement is restricted via the signal-to-noise ratio (S/N). The noise in spectrum is dealt for the deconvolution process like the bands having too low HWHM.

It is important to note that obtain an ultimate band narrowing while minimizing the noise as well as the side lobes, the initial spectrum has to be measured with the lowest feasible (S/N) ratio. And, in certain states, less high-resolution constituents throughout the range of spectrum are

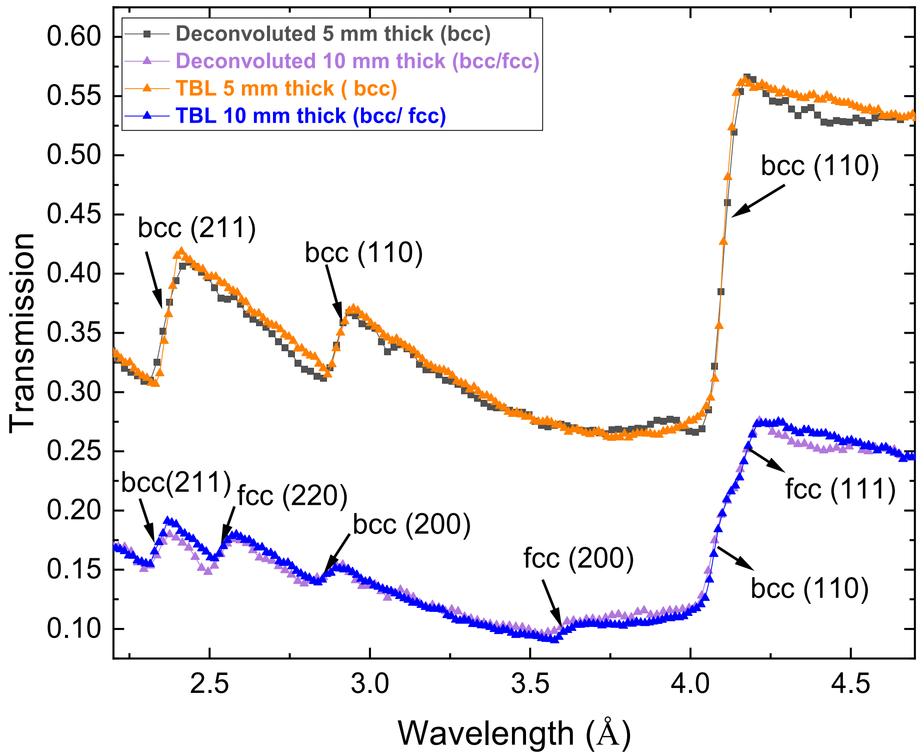

Fig. 7. The comparison between the TBL transmission spectra using a high wavelength resolution mode for both (5 mm) thickness BCC and (10 mm) entire thickness (5 mm BCC phase as well as 5 mm FCC phase behind each other) steel samples and the CONRAD-2 transmission spectra that are corrected and convoluted for the same samples. The figure displays evidence of the presence of the two phases at approximately (4.1 Å).

noticed, and as a result, less high-frequency constituents of noise in the resulting deconvolved spectrum are insignificant.

6. Experiment at a high wavelength resolution using the European spallation source test beamline (TBL)

Furthermore, using the ESS test beamline (TBL), which is based on (TOF) measurements with a chopper system design to suppress the neutron frame overlap for a specific source-to-detector distance, the information at a distance from the source based on a specially designed chopper regime, the same experiment was performed using the same sample with a higher neutron wavelength resolution (below 1%) (Strobl et al., 2013). A high wavelength resolution is needed for samples with closely spaced Bragg edges in the spectrum. The situation is quite similar to that of a powder diffraction experiment, in which the goal is to produce diffraction peaks that are both sharp and narrow.

TOF spectroscopy was carried out at the ESS V20 test beamline by employing a different chopper cascade to generate neutron pulses of varying wavelengths. The tests described here were conducted using a 2D position sensitive with a (2×3 mm^2) spatial resolution as well as a (30×30 cm^2) effective area (Kiyanagi et al., 2014). To achieve the TOF imaging studies, this detector's high time resolution for detecting cold neutrons (around a few μs) is crucial. Additional instrumentation information and technical specifications can be found elsewhere (Woracek et al., 2016).

The high-resolution neutron transmission spectra of the steel samples were registered at a detector location ($L_{det=}$47.63 m) from the source of neutron. Steel samples were selected to have varying amounts of BCC and FCC phases. The intensity of the transmission spectra was normalized by recording a measurement with no sample present to obtain the spectrum of the original beam.

Fig. 7 manifests the transmission patterns (orange and blue curves) made by the TBL instrument when it works in a high-resolution mode with a pure 5 mm thick steel with a BCC phase.

To demonstrate the Fourier deconvolution transform, Fig. 7 compares the TBL transmission spectra after the deconvolution with the spectra measured at the CONRAD-2 for several various samples of steel. The Bragg edges obtained from TBL transmission spectra are now in good agreement with those deconvoluted CONRAD-2 spectra. A shoulder-like shape for the sample containing 50% BCC (mixed phase) and 50% FCC (austenite) is now pronounced owing to the dual phase of the structure of BCC as well as FCC at roughly (4.1 Å).

Nevertheless, the wavelength resolution improvement employing the deconvolution method gives the info that the material of sample comprises two crystallographic phases. Therefore, the determined Bragg edge from the deconvolution spectra at about (4.16 Å) are currently corresponding to the data from the measurements of TBL device, as elucidated in Fig. 7.

Furthermore, the fact that the sample material contains two crystallographic phases is revealed using the deconvolution process, which improves the wavelength resolution. Fig. 7 also displays that the Bragg edges, generated from the deconvoluted CONRAD-2 spectra, now agree with the data measured at the TBL instrument observations. The wavelength resolution improved as a result of the effect of Fourier self-deconvolution, but the Bragg edges location is unaffected. The Fourier self-deconvolution's primary benefit is its ability for lowering the separate bands FWHM accurately without changing their location or overall area of band.

7. Conclusion

In this research, a method for determining the volume fractions of martensite and austenite crystals in steel has been introduced utilizing Bragg-edge neutron transmission imaging by using a Fourier deconvolution method that has been implemented, and both are user-friendly and efficient. The higher-order contamination corrections have also been applied to double-crystal monochromator devices.

The deconvolution method applied to the CONRAD-2 transmission profile is shown to improve the wavelength resolution by roughly (3%) in the transmission investigations using continuous neutron sources employing double-crystal monochromators (CONRAD-2).

The improvement of the wavelength resolution as a result of the influence of Fourier self-deconvolution doesn't affect the Bragg edges' location or shape. And, the Fourier self-deconvolution's chief benefit is that it can accurately lower the separate bands of FWHM without changing their location or overall area of band.

The deconvolution method could help to improve the spectral resolution at continuous neutron sources around the world. This could considerably broaden the types of scientific applications at continuous neutron sources and will allow the quantification of material phase and phase transformations.

Declaration of Competing Interest

The authors declare the following financial interests/personal relationships which may be considered as potential competing interests: Ala'a Al-Falahat reports article publishing charges was provided by Mutah University. Ala'a Al-Falahat reports a relationship with Mutah University that includes: non-financial support.

References

Abràmoff, M.D., Magalhães, P.J., Ram, S.J., 2004. Image processing with imageJ. Biophotonics Int. 11 (7), 36–41. https://doi.org/10.1117/1.3589100.

Ala'a, A.-F., et al., 2019. "Correction approach of detector backlighting in radiography," (in English). Rev. Sci. Instrum. Rev. Sci. Instrum. 90 (12), 125108.

Al-Falahat, A.a., et al., 2019. Energy-selective neutron imaging by exploiting wavelength gradients of double crystal monochromatorsSimulations and experiments (in English). In: Nuclear Instruments and Methods in Physics Research Section A: Accelerators, Spectrometers, Detectors and Associated Equipment Nuclear Instruments and Methods in Physics Research Section A: Accelerators, Spectrometers, Detectors and Associated Equipment, vol. 943, p. 162477.

Al-Falahat, A.M., et al., 2019. Energy-selective neutron imaging by exploiting wavelength gradients of double crystal monochromators—Simulations and experiments. In: Nuclear Instruments and Methods in Physics Research Section A: Accelerators, Spectrometers, Detectors and Associated Equipment, vol. 943, p. 162477, 2019/11/01/. doi: https://doi.org/10.1016/j.nima.2019.162477.

Al-Falahat, A.M., Kardjilov, N., Woracek, R., Boin, M., Markötter, H., Kuhn, L.T., Makowska, M., Strobl, M., Pfretzschner, B., Banhart, J., Manke, I., 2022. Temperature dependence in Bragg edge neutron transmission measurements. J. Appl. Cryst. Article 55 (4), 919–928.

Alrwashdeh, S.S., Markötter, H., Haußmann, J., Scholta, J., Hilger, A., Manke, I., 2016. X-ray Tomographic Investigation of Water Distribution in Polymer Electrolyte Membrane Fuel Cells with Different Gas Diffusion Media. ECS Trans. 72 (8), 99–106.

Alrwashdeh, S.S., Al-Falahat, A.M., Markötter, H., Manke, I., 2022. Visualization of water accumulation in micro porous layers in polymer electrolyte membrane fuel cells using synchrotron phase contrast tomography. Case Stud. Chem. Environ. Eng. 6, 100260.

Griffiths, P.R., Pariente, G.L., 1986. Introduction to spectral deconvolution. TrAC Trends Anal. Chem. 5 (8), 209–215.

Kardjilov, N., Dawson, M., Hilger, A., Manke, I., Strobl, M., Penumadu, D., Kim, F.H., Garcia-Moreno, F., Banhart, J., 2011. A highly adaptive detector system for high resolution neutron imaging. Nucl. Instrum. Methods Phys. Res. Sect. A: Accelerators, Spectrometers, Detectors and Associated Equipment 651 (1), 95–99.

Kardjilov, N., Hilger, A., Manke, I., Woracek, R., Banhart, J., 2016. CONRAD-2: The new neutron imaging instrument at the Helmholtz-Zentrum Berlin. J. Appl. Cryst. 49, 195–202. https://doi.org/10.1107/S1600576715023353.

Kardjilov, N., Hilger, A., Manke, I., 2016. Conrad-2: cold neutron tomography and radiography at BER II (V7). J. Large-Scale Res. Facilities JLSRF 2, A98–A.

Kauppinen, J.K., Moffatt, D.J., Mantsch, H.H., Cameron, D.G., 1981. "Fourier Self-Deconvolution: A Method for Resolving Intrinsically Overlapped Bands," (in English). Appl. Spectrosc. 35 (3), 271–276.

Kauppinen, J.K., Moffatt, D.J., Mantsch, H.H., Cameron, D.G., 1981. "Fourier transforms in the computation of self-deconvoluted and first-order derivative spectra of overlapped band contours," (in English). Anal. Chem. 53 (9), 1454–1457.

Kiyanagi, Y., Kamiyama, T., Kino, K., Sato, H., Sato, S., Uno, S., 2014. Pulsed neutron imaging using 2-dimensional position sensitive detectors. J. Instrum. 9 (07), C07012.

Mantsch, H.H., Moffatt, D.J., Casal, H.L., 1988. "Fourier transform methods for spectral resolution enhancement," (in English). J. Mol. Struct. 173, 285–298.

Nielsen, K., Lefmann, K., 2000. Monte Carlo simulations of neutron-scattering instruments using McStas, 2000/06/03/ Phys. B Condens. Matter 283 (4), 426–432. https://doi.org/10.1016/S0921-4526(00)00381-1.

OriginLab. SCR_014212. http://www.originlab.com/index.aspx?go=PRODUCTS/Origin (accessed).

Rahmelow, K., Huebner, W., 1996. "Fourier Self-Deconvolution: Parameter Determination and Analytical Band Shapes," (in English). Appl. Spectrosc. 50 (6), 795–804.

Strobl, M., Bulat, M., Habicht, K., 2013. The wavelength frame multiplication chopper system for the ESS test beamline at the BER II reactor - A concept study of a fundamental ESS instrument principle. Nucl. Instrum. Methods Phys. Res., Sect. A 705, 74–84. https://doi.org/10.1016/j.nima.2012.11.190.

Tötzke, C., Manke, I., Hilger, A., Choinka, G., Kardjilov, N., Arlt, T., Markötter, H., Schröder, A., Wippermann, K., Stolten, D., Hartnig, C., Krüger, P., Kuhn, R., Banhart, J., 2011. Large area high resolution neutron imaging detector for fuel cell research. J. Power Sources 196 (10), 4631–4637.

Tran, K.V., et al., 2022. Torsion of a rectangular bar: Complex phase distribution in 304L steel revealed by neutron tomography. Mater. Design, vol. 222, p. 111037, 2022/10/01/ 2022, doi: https://doi.org/10.1016/j.matdes.2022.111037.

K. V. Tran *et al.*, "Phase and texture evaluation of transformation-induced plasticity effect by neutron imaging," Materials Today Communications, vol. 35, p. 105826, 2023/06/01/ 2023, doi: https://doi.org/10.1016/j.mtcomm.2023.105826.

Willendrup, P.K., Lefmann, K., 2020. McStas (i): Introduction, use, and basic principles for ray-tracing simulations. J. Neutron Res. 22, 1–16. https://doi.org/10.3233/JNR-190108.

Woracek, R., Hofmann, T., Bulat, M., Sales, M., Habicht, K., Andersen, K., Strobl, M., 2016. The test beamline of the European Spallation Source- Instrumentation development and wavelength frame multiplication. Nucl. Instrum. Methods Phys. Res. Sect. A: Accelerators, Spectrometers, Detectors and Associated Equipment 839, 102–116.

Woracek, R., Santisteban, J., Fedrigo, A., Strobl, M., 2018. Diffraction in neutron imaging—A review, 2018/01/11/ Nucl. Instrum. Methods Phys. Res., Sect. A 878, 141–158. https://doi.org/10.1016/j.nima.2017.07.040.